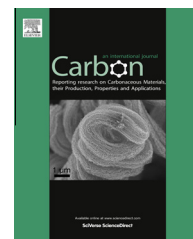


Available at www.sciencedirect.com

SciVerse ScienceDirect

journal homepage: www.elsevier.com/locate/carbon

Effect of morphology on the strain recovery of vertically aligned carbon nanotube arrays: An *in situ* study

Siddhartha Pathak^{*}, Jordan R. Raney, Chiara Daraio

Division of Engineering and Applied Science, California Institute of Technology (Caltech), Pasadena, CA, USA

ARTICLE INFO

Article history:

Received 7 March 2013

Accepted 22 June 2013

Available online 2 July 2013

ABSTRACT

We report on the distinctly different mechanical responses of two vertically aligned carbon nanotube (VACNT) films, subjected to large displacement (up to 70 μm) flat punch indentations. The VACNT films were synthesized using the same chemical vapor deposition (CVD) technique but for varying reaction times, which resulted in their different thicknesses (480 and 160 μm , respectively) and morphologies. *In situ* tests reveal that the shorter, more aligned VACNT film deforms via an instantaneous vertical shearing of the material directly underneath the indenter tip, which is manifested as a rapid displacement burst in the load–displacement response when tested at rates of 100 nm/s and above. The resultant buckles were of a more permanent nature leading to their low recoverability (22–40%). In contrast, we find the thicker, more tortuous VACNT film to show a higher (~80%) recovery and a more compliant response. These differences in the mechanical response of the VACNTs are discussed in the framework of foam-like deformation with a particular emphasis on their different morphological features, namely density and tortuosity.

Published by Elsevier Ltd.

1. Introduction

Among the wide variety of macroscopic carbon nanotube (CNT) architectures, vertically aligned carbon nanotube (VACNT) arrays have attracted special attention due to their possible applications ranging from micro-electro-mechanical systems (MEMS) to energy dissipative systems, such as visco-elastic rubbers and foams [1–6]. VACNT arrays can be readily synthesized by different techniques [7,8], and the choice of synthesis approach affects the morphology and the properties of the resulting arrays. This variability is reflected in the range of mechanical properties reported for VACNTs, such as elastic modulus and buckling strength that range anywhere from sub-MPa [6,9] to tens of MPa [10–12] to GPa [13,14] levels.

A marked difference among different VACNT arrays is the ability (or lack thereof) to recover from large deformations; with some exhibiting superior creep recovery [1,5,6,15,16], while others deform permanently even at modest strains [12,17–20]. The recoverability of VACNTs is known to depend both on the experimental loading and boundary conditions as well as on the VACNT morphology. For example, while VACNT pillars made using chemical vapor deposition (CVD) technique have been shown to exhibit near complete (~95%) recovery under uniaxial compression [16], the same VACNT microstructure showed negligible – almost zero – recovery under flat-punch indentation experiments [21,22]. It has been suggested that the different boundary conditions present in indentation experiments can result in significant shear stresses in the material – this causes the VACNT films to deform by an instantaneous vertical shearing of the material directly

^{*} Corresponding author. Present address: MPA-CINT Center for Integrated Nanotechnologies, Los Alamos National Laboratory, P.O. Box 1663, MS-K771, Los Alamos, NM 87545, USA. Fax: +1 (505) 665 9030.

E-mail addresses: pathak@caltech.edu, siddharthapathak@gmail.com (S. Pathak).

0008-6223/\$ - see front matter Published by Elsevier Ltd.

<http://dx.doi.org/10.1016/j.carbon.2013.06.083>

underneath the indenter tip, and the permanent nature of the damage caused by shearing severely compromises the recoverability of the VACNTs [22,23]. The recoverability of VACNTs has also been shown to depend on the VACNT microstructure and morphology. In general, researchers growing CVD-VACNTs made using the ‘floating’ catalyst route [24,25] have reported substantial (>90%) recovery in their samples [1,25–27], while the recoverability of majority of VACNTs made using the ‘fixed’ catalyst technique [20,28] has been poor [12,17–19] (note: Ref. [16] is a notable exception). This effect is thought to be correlated to the thicker (>40 nm) diameter of the tubes, and a correspondingly higher density for VACNTs made using the floating catalyst route. A systematic study by Bradford et al. [29] analyzed this effect further, where it was shown that VACNTs grown using a fixed catalyst technique and exhibiting low resilience changed to an almost complete recovery after a post growth CVD treatment. This was attributed to an increase in the individual CNT wall thickness, which also caused increased surface roughness of the CNTs, resulting in a decrease of the van der Waals interactions.

Other aspects of the VACNT microstructure are also known to influence their mechanical properties, such as their tortuosity (or waviness) and the number of inter-tube junctions in the matrix. A few studies have attempted to explore these effects experimentally [30–33], but no strong correlations were observed. Some key insights into these parameters can be gained from the theoretical studies involving random network of stiff fibers. For example, Astrom et al. [34] have applied their modified semi-theoretical version of the Cox shear-lag model [35] to CNT mats and fibers, while taking into account the statistical number of bundle–bundle contacts. Their study suggests a linear relationship between the number of contact points and the modulus of the CNT network. A similar result was also obtained by Berhan and coworkers [36], who also found that an increase in the waviness of the nanotube ropes results in a significant decrease in their effective modulus [37].

The lateral interaction of the nominally aligned CNTs is also an important parameter for determining the mechanical behavior of the VACNT array (such as compressive modulus [32]), and it has been observed to vary with total array height, with taller arrays often showing more lateral entanglement [38]. Arrays as short as 50 nm [39] and as long as several mm [13] have previously been examined. The mechanical responses of these extreme cases have been very different, with the short sample being made up of non-interacting parallel CNTs and the long sample consisting of highly entangled CNTs.

Such drastic changes in the VACNT properties make it impractical to compare the performance of VACNTs synthesized by non-identical growth techniques. In this work, we focus on VACNT films of two different heights of 160 and 480 μm respectively, which were grown by the same floating catalyst CVD technique [24,25] and exhibit a highly entangled morphology. Using flat punch diamond indenter tip geometries we perform large displacement instrumented indentation experiments to characterize the mechanical behavior of the two VACNT films. Compared to other indenter tip geometries,

the contact area for a flat punch indenter does not change with displacement. This is especially advantageous for the unique microstructural hierarchy of VACNT films, where the micrometer-to-millimeter sized film is composed of millions of individual nanotubes with diameters in the nanometer range. Such an arrangement not only renders the mechanical response of VACNTs to be distinct from monolithic materials, but also poses a challenge in the accurate estimation of the contact area between the VACNT film and the commonly used parabolic [14,40] and pyramidal [40] indenter tip geometries. The constant contact area between the flat punch indenter and the VACNT sample is also of advantage in measuring the viscoelastic response of the VACNT assembly.

We utilize both an *in situ* nanoindentation methodology to observe the on-edge deformation in real time using a custom-built *in situ* nano-mechanical deformation instrument, SEMentor [41], as well as more traditional *in-bulk ex situ* indentation methods in this work. The *in situ* tests conducted inside the scanning electron microscope (SEM) have the advantage of allowing uninterrupted observation of the real-time evolution of deformation while simultaneously recording load vs. displacement data, thus providing a one-to-one correlation between the morphological changes and the mechanical response [17,21,42]. However, in order to facilitate an uninhibited view of the material cross-section, *in situ* indentation experiments need to be conducted on the edge of the sample [21]. While such a set-up causes the boundary conditions and constraints to differ from those during *in-bulk* indentations, they provide important information on morphological evolution during deformation of VACNTs, not easily obtainable by other methods.

2. Materials and methods

2.1. CNT growth

Aligned CNTs were synthesized on thermally oxidized Si wafers using vapor phase (or “floating catalyst”) thermal CVD techniques that have been in wide use for more than a decade [24]. Synthesis took place at atmospheric pressure in an inert Ar atmosphere at 827 °C. A precursor solution of ferrocene (which pyrolyzes to release atomic Fe to act as a catalyst for CNT growth) and toluene (which acts as a carbon source) was created at a concentration of 0.02 g ml⁻¹ and injected at approximately 1 ml min⁻¹ into the heating zone of the furnace in a flow of 800 sccm of Ar. The quartz furnace tube had a diameter of approximately 4 cm and the heating zone was about 20 cm long. VACNT samples of different heights were generated by varying the amount of precursor solution used (and hence the total reaction time). Two VACNT samples, of film thicknesses 480 and 160 μm and named samples A and B, respectively, were selected for further study. The longer sample corresponded to 10 ml of precursor solution and the shorter sample to 7 ml of precursor solution (about 10 and 7 min total reaction time, respectively). All other synthesis parameters between the samples were unchanged. Large portions of the samples ($\sim 10\text{ mm}^2$) were removed from the substrate with a razor blade, and their masses were obtained with a microbalance. Sample densities were ob-

Table 1 – Comparison between Samples A and B. The uncertainty in the density values is around 10%. The CNT diameters are average \pm standard deviation values from the top portions of the VACNT films.

	Sample A	Sample B
Synthesis time	10 min	7 min
Height	480 μm	160 μm
Density	0.13 gm/cm^3	0.06 gm/cm^3
CNT dia	68.1 \pm 10.6 nm	31.1 \pm 7.5 nm

tained by dividing these measured values of mass by the respective volumes of the sample portions (with film thickness determined by scanning electron microscope (SEM) and areal dimensions directly obtained with calipers). Table 1 lists the major differences between samples A and B. The samples were studied using both SEM (FEI Nova 200 and 600, FEI Quanta 200) and transmission electron microscopy (TEM, FEI TF30UT) machines as shown in Fig. 1. Note the localized regions of lower density, visible as horizontal bands along the height of the VACNT structure in sample B in this figure.

Although both samples were synthesized under very similar conditions, we noted significant differences in their morphological features, and therefore in their mechanical

behavior. These differences arise due to subtle effects related to the injection of our precursor solution. For example, modest increases in carbon concentration in the reactor can lead to increased entanglement of the individual CNTs [43]. Similarly, because CNT diameter depends on injection rate of the precursor solution [44], fluctuations in this rate can lead to localized regions of lower density, visible as horizontal bands along the height of the final VACNT structure [45]. We have observed in the past that these regions can result in strain localization during compression [45]. Fluctuations in both of these quantities are especially likely at the beginning of our growth process due to variability that occurs during the sudden injection of a precursor solution. Because of the bottom-up growth process by which our VACNTs are synthesized [46,47], these fluctuations at the beginning of the growth process are reflected in morphological differences near the top of the VACNT array (i.e., where the oldest growth is present). Note that under indentation the majority of the indentation stresses are also localized at the top portions of the VACNT array.

In order to test the repeatability of the samples, we synthesized a third set of VACNT samples with the lower reaction time of 7 min. While this sample set was similar in thickness ($\sim 170 \mu\text{m}$) to sample B, it did not contain any bands of lower VACNT density as seen in sample B. The detailed results for this third sample set are not shown in this paper.

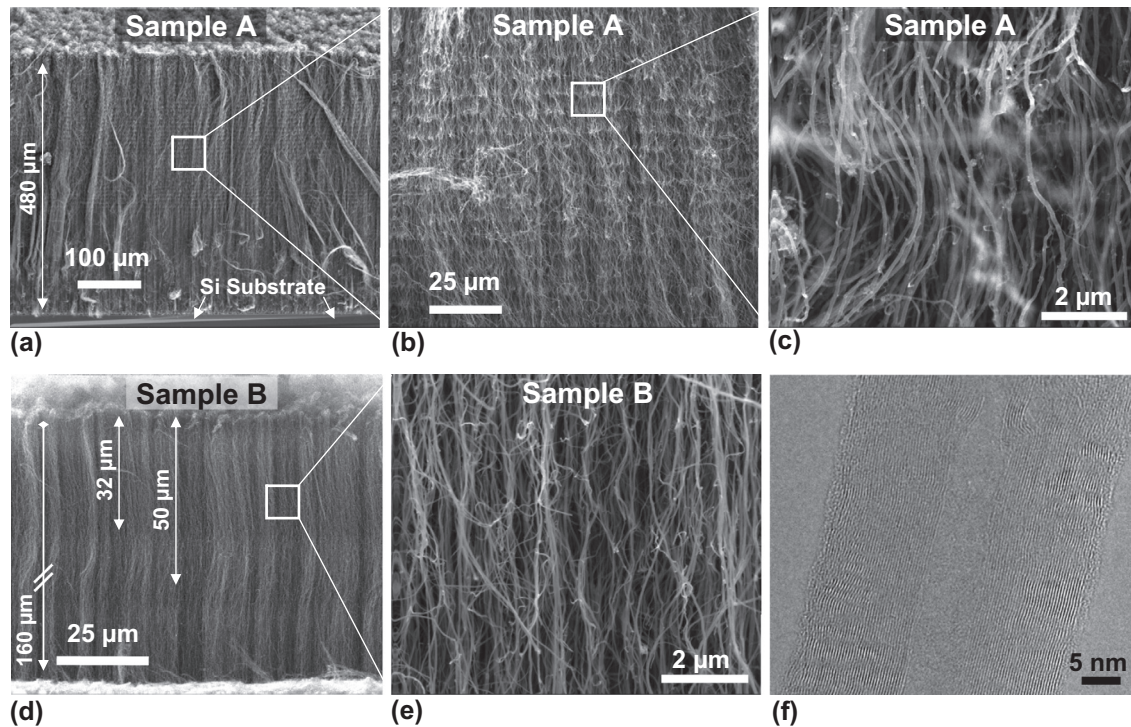


Fig. 1 – SEM images reveal the hierarchical morphology of the (a) 480 μm thick VACNT films (Sample A), which consist of (b) horizontal layers of high tortuosity, and (c) a complex intertwined network of nominally vertical CNTs at higher mag. (d) On the other hand, a lower thickness VACNT film (Sample B, only top portion of the 160 μm film is shown) shows (e) a more aligned CNT structure at high mag. Note the dark bands at $\sim 32 \mu\text{m}$ and $\sim 50 \mu\text{m}$ from the top in Sample B suggesting regions of lower density in (d), as well as the lower wall thickness of the CNTs in Sample B (compare (c) and (e)). SEM pictures (a), (b), (c) and (e) are taken at a 60 deg tilt angle while (d) is at 86 deg tilt. (f) Individual multiwalled CNTs are visible in the TEM image.

2.2. Ex situ indentations

We tested the two different VACNT films with thicknesses of 480 and 160 μm (samples A and B) under large displacement cyclic indentation tests. The indentation experiments were performed using the XP module of Agilent's nanoindenter G200 with adjustable software control methods, as described in Ref. [17]. Tests were performed in air using a custom made cylindrical diamond flat punch with $\sim 120 \mu\text{m}$ diameter and $\sim 80 \mu\text{m}$ height. Indentations were performed under a constant displacement control varying indentation depths up to a maximum of around 70 μm (restricted by the height limitations of the diamond flat punch). Tests were conducted in the interior of the samples ('in-bulk' tests, i.e., away from the sample edge) at three different constant displacement rates: 10 nm/s, 100 nm/s and 1000 nm/s. Typically 5 load-unload cycles were performed at each displacement level. No hold time was applied at the maximum loads, and each cycle was unloaded to only 10% of the max load in the previous cycle, in order to maintain the cyclic nature of the tests. A minimum of 10 tests were conducted at each displacement rate. The indents were spaced at least 500 microns apart in order to eliminate any possible proximity effects.

2.3. In situ SEM indentations

In situ tests were conducted in a custom-built indentation instrument [41], composed of a nano-mechanical dynamic contact module (Agilent Corp.) inside a SEM (Quanta 200, FEI). Tests were conducted on the sample edge ('on-edge' [22] experiments, to facilitate viewing) with a conductive diamond flat punch with a rectangular flat cross-section of $\sim 60 \mu\text{m} \times 80 \mu\text{m}$. The loading axis in the instrument is inclined at $\sim 86^\circ$ with respect to the electron beam, thus allowing continuous observation of the deformation morphology of the VACNT film cross-section during the on-edge in situ experiments. SEM observations were recorded as a video file at 30 frames per second and synchronized with the indentation data to provide a real-time correlation between each video frame and the corresponding position on the load-displacement curve. Three video files are provided as supporting on-line material – video file [Supplementary video S1](#) shows the on-edge indentation on sample A conducted at a 100 nm/s displacement rate, files [Supplementary video S2](#) (at 100 nm/s displacement rate) and [Supplementary video S3](#) (at a slower 10 nm/s displacement rate) show the same for sample B. These three video files are shown at 30, 25, and 250 times their original speeds, respectively. These tests were conducted to a maximum penetration depth of 30 μm (instrument limit).

While both the *ex situ* and the *in situ* experiments are nominally identical, some differences exist. First, the *in situ* tests are conducted in a vacuum environment vs. the *ex situ* tests, which are conducted in air. Moreover, in the *in situ* case the samples are constantly exposed to the electron beam, and they are oriented horizontally such that gravity is acting perpendicular to the compression axis. Also as described earlier, the outer constraints in on-edge indentations are different from those during in-bulk tests, and therefore the measured mechanical behavior is expected to be different. Hence, all

data analyses were performed only on tests conducted in air in the *ex situ* nanoindenter; the *in situ* results are used here for visualization purposes only.

2.4. Data analysis

The applied load, P , and measured displacement, h , were corrected for machine compliance following the procedure outlined in detail in Ref. [17]. The unloading modulus was calculated from the initial unloading segment of the measured load-displacement curve using Hertzian contact mechanics [48,49] and assuming negligible friction between the indenter sidewalls and the VACNT matrix [50–52] as:

$$E_{\text{eff}} = \frac{\sqrt{\pi}}{2} \frac{S}{\sqrt{A}} = \frac{S}{2a}, \quad \frac{1}{E_{\text{eff}}} = \frac{1 - \nu_s^2}{E_s} + \frac{1 - \nu_i^2}{E_i} \quad (1)$$

where E_{eff} denotes the effective modulus of the combined indenter-specimen system; $S (= dP/dh)$ is the stiffness measured from the slope of the initial 30% of the unloading load-displacement curve; ν and E are the Poisson's ratio and the Young's modulus, respectively; and the subscripts s and i refer to the specimen and the indenter, respectively, with $E_i = 1041 \text{ GPa}$ and $\nu_i = 0.07$. A vanishing Poisson's ratio of $\nu = 0$ was assumed for the VACNTs [53]. Unfortunately, due to misalignment issues between the indenter tip and the sample surface Eq. (1) cannot be applied to the initial loading portion of the test. Eq. (1) is also limited by the inherent assumptions of Hertz' theory, which assumes an isotropic, elastic, continuum material behavior. VACNTs, on the other hand, demonstrate varying degrees of anisotropy at each level of its hierarchical microstructure (see Fig. 1). Thus, our measurements of VACNT indentation moduli should instead be treated as their equivalent continuum isotropic values. We also point out that this isotropic continuum framework has been previously utilized in developing the constitutive relations in VACNTs [17] and foams [54], and appears to have accurately captured the qualitative features of their outer deformation profiles and the stress-strain responses. The continuum foundation is also motivated by the nearly isotropic network of CNTs as revealed by images at or above magnifications of 30,000 \times (Fig. 1c and e).

We define the percentage recovery (R) as the displacement recovered at the end of each cycle with respect to the maximum displacement, i.e.

$$R = \frac{h_{\text{max}} - h_{\text{unload}}}{h_{\text{max}}} \quad (2)$$

where h_{max} is the maximum displacement at the end of loading and h_{unload} is the displacement after unloading to 10% of the max load in each cycle.

The loss coefficient, η , (a dimensionless quantity) measures the degree to which a material dissipates energy and is calculated as [55]

$$\eta = \frac{\Delta U_i}{2\pi U_1}, \quad U = \int_0^{\sigma_{\text{max}}} \sigma_{\text{ind}} d\varepsilon_{\text{ind}} \approx \frac{1}{2} \frac{\sigma_{\text{max}}^2}{E_s}, \quad \Delta U = \oint \sigma_{\text{ind}} d\varepsilon_{\text{ind}} \quad (3)$$

where U_1 is the elastic energy stored in the material when it is loaded elastically to a stress σ_{max} in the 1st cycle, ΔU_i is the energy dissipated in the i^{th} load-unload cycle, and σ_{ind} and ε_{ind} denote the sample's stress and strain under indentation.

2.5. Viscoelastic characterization

The viscoelastic properties of the VACNT films were measured following the procedure outlined in Ref. [17]. In this method, the indenter is loaded into the sample in air at a constant displacement rate of 100 nm/s up to a specified indentation depth, at which point the indenter head is oscillated at ~8 nm amplitude across a range of frequencies from 1 to 50 Hz. The cut-off frequency of 50 Hz is dictated by the instrument limit, as detailed in Refs. [17,56]. The procedure was repeated at six different constant indentation depths for sample A: 15, 26, 36, 47, 58 and 68 μm , respectively. In sample B, however, the viscoelastic properties could be measured for only the three deeper indentation depths of 47, 58 and 68 μm . As described in the next sections, there is a large ~30 μm displacement burst in sample B during loading, which masks the viscoelastic measurements at the lesser depths.

Viscoelastic materials are commonly characterized by their storage (E') and loss (E'') moduli, as well as the ratio of the two $\tan \delta$. E' represents the stored energy or the elastic response, and E'' corresponds to the amount of energy dissipated, or the viscous response. Assuming linear viscoelastic behavior, these terms can be computed following the calculations described in Refs. [56–59] as follows:

$$E' = k' \frac{\sqrt{\pi} (1 - \nu_s^2)}{2\beta \sqrt{A}}, \quad k' = \left| \frac{F_0}{u_0} \right| \cos \varphi - \left| \frac{F_0}{u_0} \right|_{\text{air}} \cos \varphi_{\text{air}},$$

$$E'' = k'' \frac{\sqrt{\pi} (1 - \nu_s^2)}{2\beta \sqrt{A}}, \quad k'' = \left| \frac{F_0}{u_0} \right| \sin \varphi - \left| \frac{F_0}{u_0} \right|_{\text{air}} \sin \varphi_{\text{air}}, \quad \tan \delta = \frac{E''}{E'}. \quad (4)$$

Here k' and k'' are the storage and loss stiffnesses of the sample, obtained by finding the real and complex parts, respectively, of the stiffness differences between oscillating the indenter head on the sample at a fixed displacement and in air at the same raw displacement, β is a constant (=1 for a flat punch indenter). F_0 and u_0 are the load and displacement oscillation amplitudes, respectively, and φ is the phase angle between the load and displacement oscillations. We note that the accuracy in the values of E' and E'' in Eq. (4) can be affected by several factors: uncertainties in Poisson's ratio, since it may be frequency dependent, and ambiguity in contact area, especially at shallower indentation depths, where full contact may not have been established. On the other hand, calculation of $\tan \delta$ is independent of the contact area, and thus is ideally suited as a measure of the viscoelasticity of the indented material [14,60].

3. Results and discussion

3.1. VACNT morphology

The complex hierarchical nature of the VACNT microstructure, with distinct organizational details across multiple length scales, is shown in Fig. 1a–c (sample A) and Fig. 1d and e (sample B). Thus, while VACNTs appear as continuous films at lower magnifications, the nominally vertical alignment of CNT bundles growing perpendicularly to the support substrate is apparent at a higher magnification of 500 \times and above (Fig. 1a and d). Still higher magnifications of 30,000 \times reveal significant intertwining in the long, curved lengths of individual CNTs along the VACNT height, and at this length

scale the CNT network appears more isotropic [17,54,61] (Fig. 1c and e). A representative image, obtained via TEM, of the internal structure of an individual multiwall (typically 20–60 walls) CNT is shown in Fig. 1f. As a result of this complex hierarchical structure, the mechanical behavior of the VACNT matrix depends both on the properties of individual CNTs, as well as their mutual interactions and distribution throughout the array.

Fig. 1 and Table 1 also highlight some of the important morphological differences between samples A and B. The cross-sectional view of Sample A in Fig. 1a indicates that the CNTs in the top 290 μm height of this sample are highly tortuous. The expanded views of this region in Fig. 1b and c shows that the tortuous CNT bands have a uniform chord length (straight line distance between the ends of two neighboring tortuous regions) of around 7.5–8 μm throughout this height.

The CNTs seen in the shorter (~160 μm tall) sample B have negligible tortuosity and follow relatively straighter paths (Fig. 1d and e). Note that the bottom ~180 μm of sample A also does not show any major tortuosity. As described in Section 2, both VACNT samples were synthesized using the same nominal CVD growth conditions, but for different reaction times. The top portions of the samples thus reflect the regions of oldest growth in each case (CVD is essentially a bottom-up growth process). Since tortuosity is present only in the taller sample, it would seem to indicate that the alignment of individual CNTs in VACNT arrays is related to the CVD growth time (and hence the VACNT height) [47]. Such tortuous paths along a CNT are capable of storing more elastic energy than straight paths.

Sample B also shows the presence of two dark bands in its cross-section. The first of these bands is seen at a distance of ~32 μm from the top surface, while the second one is at ~50 μm (Fig. 1d). As described earlier, these bands develop due to fluctuations in the input rate of the precursor solution [45]. The density of the CNTs in these banded regions is known to be lower than the average [62], and hence these regions are expected to have a softening effect on the overall microstructure [45].

A closer inspection of the top regions of samples A and B also indicate that the CNTs are of much larger diameter in sample A as compared to B (compare Fig. 1c vs. e). This effect has been described in detail in Ref. [63] where the CNT wall thickness increases as a function of the growth time. The average and standard deviation values of the CNT diameters provided in Table 1 indicate that the tubes in the upper region of sample A (CNT diameter 68.1 ± 10.6 nm) are twice as thick as that of sample B (diameter 31.1 ± 7.5 nm). As an obvious consequence of the difference in their tube diameters, sample A also has larger density than sample B (Table 1).

3.2. In situ on-edge flat punch indentations

The different microstructures of the two VACNT samples A and B also result in distinct mechanical responses under indentation. This can be seen in the *in situ* SEM indentations described in Fig. 2. Fig. 2c compares the load–displacement responses of the two on-edge tests between samples A and B. The following points are immediately evident from this figure: (i) The slope of the initial loading segment of the

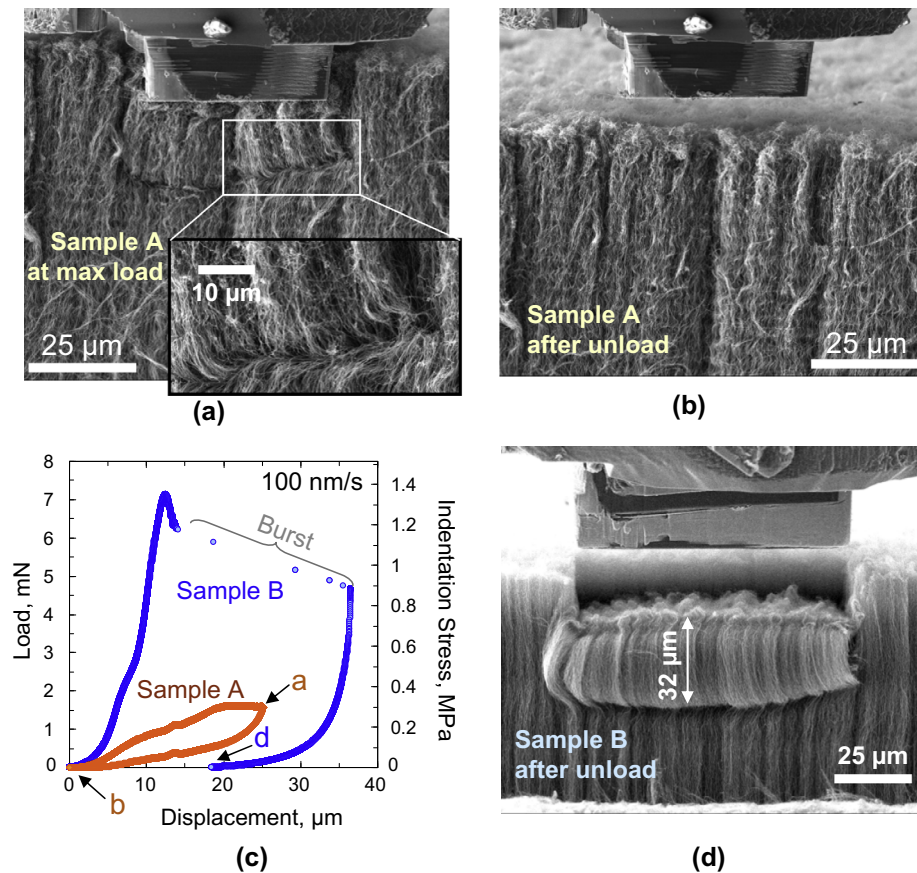


Fig. 2 – In-situ SEMentor observations of on-edge indentations on (a) Sample A at maximum load, (b) Sample A after unload, and (d) Sample B after unload. Their corresponding locations on the load-unload cycles at 100 nm/s loading rate is shown in (c). All SEM images were taken at 86 deg tilt angle. These snapshots were captured from video files S1, S2 and S3.

load–displacement curve is significantly larger for sample B, indicating a much stiffer response for sample B than for sample A. (ii) In sample B the initial loading is followed by a sudden instability at a load level of 6.2 mN, manifested by a large displacement burst of length $\sim 22 \mu\text{m}$. No such burst is seen in sample A. (iii) Upon unloading, sample A shows almost full recovery, while sample B shows a much lower ($\sim 49\%$) recovery (compare Fig. 2a and b (sample A) vs. Fig. 2d (sample B)).

The video files for these two on-edge indentation tests, which correlate the morphological changes happening in the samples under the indenter with their respective load–displacement responses, are provided as supporting online materials (video files *Supplementary videos S1 and S2*), with several representative snapshots shown in Fig. 2a, b and d. For sample A (video file *Supplementary video S1*), the sequence of events occurring during the *in situ* indentations show that at the onset of indentation CNTs in the topmost $\sim 14 \mu\text{m}$ of the VACNT film start to bend. As the indenter tip pushes forward, shear lines appear at the corners of the flat punch indenter. Further penetration of the indenter results in the formation of a buckling zone $60 \mu\text{m}$ directly below the indenter (see Fig. 2a inset). Note that the deformation of the VACNTs under indentation appears to be highly localized. Similar to foam deformation, the indentation zone for VACNTs is confined to the region directly beneath the indenter,

while the surrounding regions are unaffected. This has generally been attributed to the non-existent Poisson's ratio in structures such as open-cell foams and VACNTs [18,54,64,65], and is very different from the hemispherical indentation plastic zone reported under monolithic materials [66]. Unloading of the indenter tip reveals a remarkable resilience in the VACNTs in sample A, and hardly any after-effects of the indentation pressure can be seen on the surface of the VACNT film after full unload (compare Fig. 2a vs. b).

In contrast, the initial loading in sample B (video file *Supplementary video S2*) is followed by a small drop in indentation load (from 7.1 to 6.2 mN), after which a sudden and extensive displacement burst occurs. SEM images obtained immediately after this burst (SEM scanning rate was not fast enough to catch the details during the instantaneous burst) reveal that the top portion of the VACNT film has sheared off vertically below the edges of the indenter tip (Fig. 2d). The shear appears to be the result of a single buckle formed at a height of $\sim 32 \mu\text{m}$ from the top of the VACNT film. The shear burst causes the indenter head to momentarily lose contact with the VACNT film, presumably since the VACNT film is collapsing at a faster rate than the prescribed motion of the indenter head (gravity cannot be responsible for the burst since gravity is acting perpendicular to the indentation axis). Interestingly, the $32 \mu\text{m}$ distance also corresponds to the location of the

zone of dark bands seen in the cross-sections of these films (see Fig. 1d). As described earlier, these dark regions are known to be zones of lower density in the VACNT matrix, and thus are predicted to be the first regions to buckle.

We find that the occurrence of the displacement burst in sample B depends strongly on the applied displacement rate. Indentation tests at slower displacement rates of 10 nm/s (video file S3) did not show any discrete behavior such as bursts, etc. Instead, we observe a gradual drop in the load from 6.2 to 3.2 mN after the onset of buckling. This would seem to indicate that at the lower displacement rates the individual CNT struts have enough time to realign themselves so as to avoid a catastrophic burst phenomenon [16]. As in the case of the faster tests, the buckling zone for the slower tests also coincides with the zone of lower density VACNTs at $\sim 32 \mu\text{m}$ from the top of the VACNT film. Further loading beyond the load drop at the slow displacement rate results in a flat plateau region where the displacement increases at a constant load. The SEM recordings of this stage indicate that the indenter is now pushing down on a rectangular region of width equal to the indenter tip and bounded at the bottom by the buckled zone (of height $\sim 32 \mu\text{m}$).

The buckles formed in sample B (for both the slow and fast indentation rates) are of a more permanent nature, and unloading of the indenter tip results in a much lower recovery for sample B than what was seen for sample A (Fig. 2d).

While the general pattern of deformation seen in the *in situ* videos (Fig. 2) is similar to those of typical open-cell foams, the shear events and the recoverability are unique characteristics seen only in intertwined VACNT systems. In VACNTs the plastic strain under the indenter is accommodated entirely by the formation of the lateral folds or buckles, which are highly localized. This is in contrast to traditional foams, where cell-edge bending and cell collapse are primarily responsible for the elastic–plastic foam response [65,67]. Similarly, a shear event in non-interacting VACNTs [68] would propagate through the entire thickness, thus severely limiting its recoverability. The two examples shown in Fig. 2 demonstrate how the different degrees of alignment and intertwining between the individual CNTs affect the ability of the VACNT array to recover from large indentation strains.

3.3. Ex situ in-bulk large-displacement indentations

In order to analyze the VACNT deformation beyond the displacement limit of the *in situ* tests, *ex situ* indentation tests were conducted in air in the Agilent G200 nanoindenter to larger depths of $\sim 70 \mu\text{m}$ in the interior of the as-grown VACNT film away from the edges ('in-bulk' tests, see Section 2). This maximum indentation depth is limited by the height of the cylindrical indentation punch ($\sim 80 \mu\text{m}$). Fig. 3a shows a comparison of the indentation load (stress)–displacement responses of two representative in-bulk tests between samples A and B, conducted at a displacement rate of 10 nm/s. For both samples, three distinct regions are apparent from Fig. 3a: (i) a short elastic regime, followed by (ii) an instability with an accompanied load drop suggesting the onset of buckling, and (iii) a subsequent plateau region. The plateau region can be further subdivided into two separate sections: an initial relatively flat section (where the load is more-or-less constant with

increasing displacement) followed by a positively sloped hardening section, where the load increases more rapidly with displacement and contains several undulations. As expected, the in-bulk tests show significantly higher loads than those of the on-edge tests (compare Figs. 2c and 3a) due to the more restrictive boundary conditions in the in-bulk setup.

Fig. 3a also shows the effect of unload-reload cycling and hysteresis [14] in the VACNTs. We show 5 load-unload cycles for each sample. As seen from this figure, the first cycle is distinctly different from all subsequent loading cycles [1,2,42]. Subsequent cycling also results in a substantially higher relative recovery as compared to the first. In some cases during unloading we also measured the applied loads to be slightly negative, likely due to the adhesive interactions between the VACNTs and the diamond indenter tip [10,61].

A comparison of the load–displacement curves in Fig. 3a reveals some important differences between the indentation response of VACNT samples A and B. As in the case of the *in situ* on-edge tests, the in-bulk tests also show a much stiffer response for the VACNT sample B as compared to sample A. This is reflected in the higher slope of the initial loading segment, and in the higher resistance to buckling for sample B. In general the indentation loads (and stresses) are seen to be significantly higher for sample B than for sample A at equivalent indentation depths. We calculate the indentation stress at the point of instability (σ_{ins}) to be $\sim 0.9 \text{ MPa}$ for sample B, which is twice as high as that for sample A ($\sigma_{\text{ins}} = 0.44 \pm 0.04 \text{ MPa}$). There is a steep drop in indentation load immediately following the instability. The load drop is larger for sample B (from 10.4 mN to 6.7 mN) than for sample A (from 5.3 mN to 4.9 mN). As seen earlier from the *in situ* tests (video file Supplementary video S3) the load drop signifies the onset of buckling of the VACNTs under the indenter. Particularly in the case of sample B, the *in situ* tests revealed the buckling to originate at the zone of lower density (seen as a dark band in Fig. 1d) which is located at $\sim 32 \mu\text{m}$ below the top surface.

Sample B also shows a pronounced flat plateau region of constant stress following the load drop. As in the *in situ* tests (see video file Supplementary video S3), this flat plateau is a likely result of the continuous buckling of the VACNTs under the indenter within a height of $\sim 32 \mu\text{m}$ (i.e. up to the first VACNT band of low density). As expected, the flat plateau ends after around $30 \mu\text{m}$ of displacement, and is followed by a steep increase in the indentation load as the indenter experiences the denser VACNTs underneath.

Such sloped plateau regions have been observed previously in VACNTs [1,16,25], and an inherent property gradient in the VACNT microstructure along its height has been generally suggested as the cause. The particular constraints and boundary conditions under indentation loading, where the indenter continuously samples an increasing material volume, as well as a progressive densification of the VACNT matrix with increasing indentation depth, could also cause such a sloped region [14,22]. A combination of all of these effects is thought to be responsible for the features seen in Fig. 3a, where the indenter encounters a denser, and hence stiffer, material in the deeper regions leading to an increasing global slope in the plateau region.

The later section of the plateau region for sample B also shows a large undulation or kink at around $\sim 50 \mu\text{m}$ of

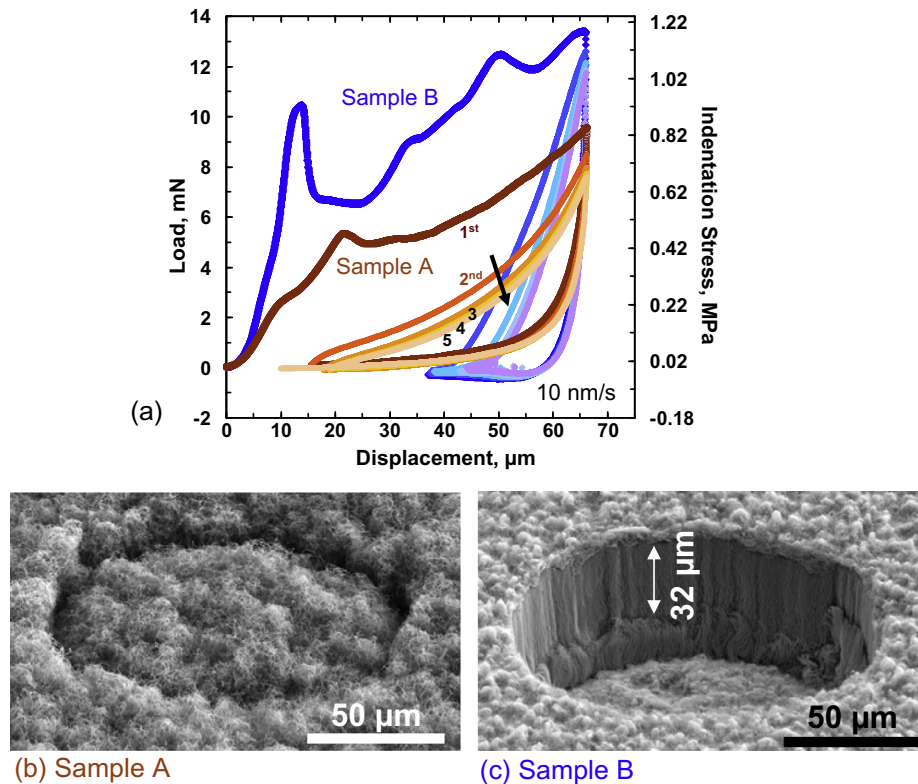


Fig. 3 – Indentations in the bulk of the sample, away from edge effects. (a) Comparative indentation load (stress) – displacement cycles (5 cycles each) for VACNT samples A and B. Loading at 10 nm/s loading rate shows 3 distinct regimes; elastic, a drop in load at a critical instability stress and plateau regime. Successive load-unload cycles to the same maximum displacement reveal a gradual drop in recovery in every cycle, suggesting progressive damage accumulation in the material. The corresponding indentation stress values are shown along the secondary y axis. Residual imprints of flat punch indentation are shown for (b) Sample A and (c) Sample B.

indentation depth (Fig. 3a). This distance matches well with the location of the second band of lower density in sample B (see Fig. 1d). No such instabilities are observed in sample A.

Unloading from a depth of $\sim 65\text{--}70\ \mu\text{m}$ results in a much higher recovery for sample A than for sample B, as shown by the images of the residual imprints (Fig. 3b and c respectively). The imprint for the VACNT sample B (Fig. 3c) also shows the remnant of the zone of low VACNT density, which is seen as a shear line at a depth of $\sim 32\ \mu\text{m}$ along the walls of the crater. The vertical walls of the indent imprint above this depth indicate a clear shearing of the VACNTs in this height and thus possibly a lower degree of entanglement among the VACNTs for sample B. These images also help to show the highly localized nature of the VACNT deformation, where all of the deformation is limited to the vertical shear region along the rim of contact between the sample and the indenter tip.

We note that at loading rates faster than 10 nm/s the plateau region is obscured by a large displacement burst, particularly for VACNT sample B (a similar effect was noted earlier in the *in situ* tests as well in Fig. 2c). In these cases a rapid, extensive displacement burst of $\sim 30\ \mu\text{m}$ was noticed immediately after attaining σ_{ins} at the faster loading rates of 100 and 1000 nm/s. Unlike the gradual drop in load seen in Fig. 3a, such a burst indicates a temporary loss of contact between the sample and the indenter tip. Based on the *in situ* indentation tests described in Fig. 2, it appears that the burst may be

caused by a rapid vertical shearing of the material directly underneath the indenter tip along the indenter edges up to a depth of $\sim 32\ \mu\text{m}$ (i.e. up to the location of the first low density zone). This was verified by stopping the test at the moment of the burst, which resulted in an imprint mirroring the shape of the indenter and of depth $\sim 32\ \mu\text{m}$.

3.4. Analysis of indentation response

Fig. 4 shows a summary of the results from the in-bulk tests on VACNT samples A and B (*in situ* on-edge tests are not included in this summary). The unloading modulus, defined in Eq. (1), is plotted as a function of the maximum displacement before unloading in Fig. 4a. Results are shown for three different loading rates – 10, 100 and 1000 nm/s. For sample B, the results are also segregated by whether they are measured before (open symbols) or after (filled symbols) the first instability.

Fig. 4a shows that in sample B, the changes in the unloading moduli clearly reflect the softening effects of the zones of lower density present along the height of the VACNT film. As shown in Fig. 1d, two such zones were visible in the cross-sectional view of VACNT sample B: at ~ 32 and $\sim 50\ \mu\text{m}$ below the top surface, respectively. The unloading moduli for sample B also show two sharp drops just before these displacement levels, as shown by the trend line for the 1000 nm/s tests. The first stiffness drop ($\Delta E_s \approx 170\ \text{MPa}$ at around $20\ \mu\text{m}$

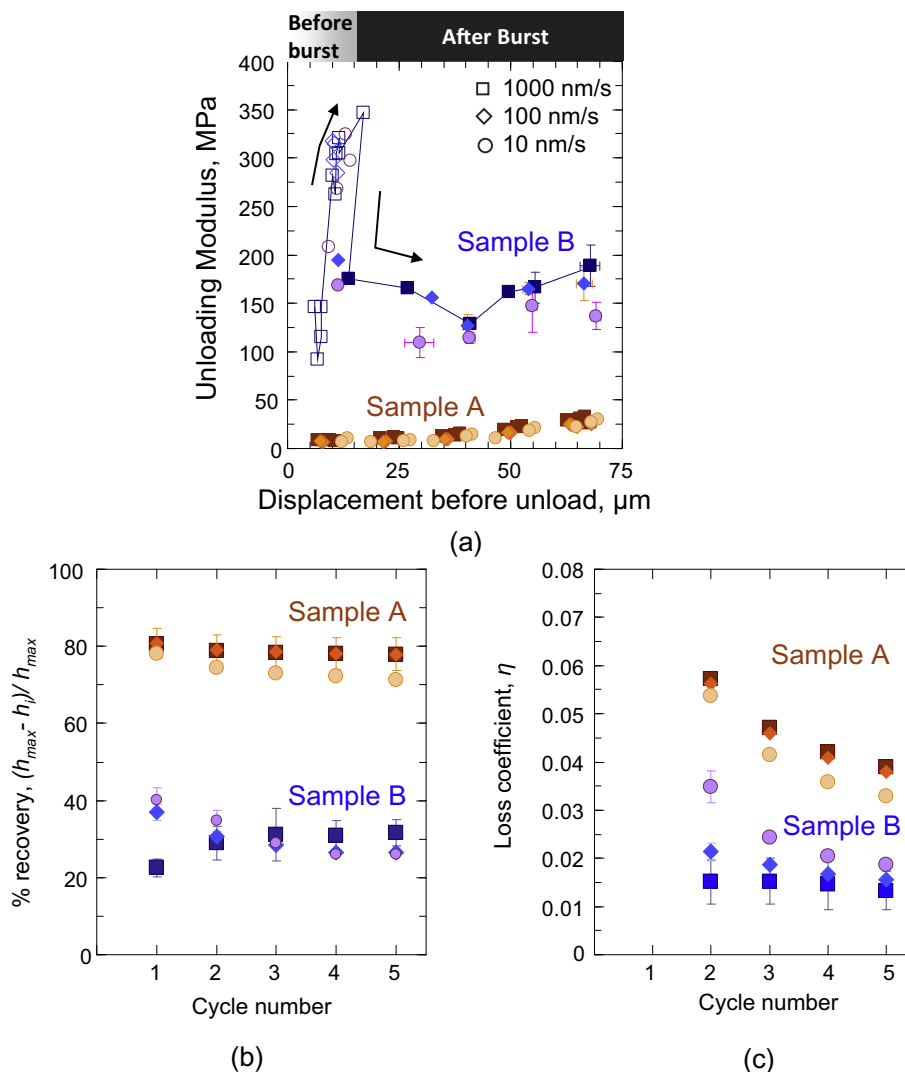


Fig. 4 – (a) Unloading modulus as a function of max displacement before unload for three different loading rates. For sample B the open symbols represent values before the first instability (burst) during indentation loading of this sample, while the filled symbols are for the values after the instability. (b) % recovery and (c) loss coefficient – both calculated at large indentation depths (i.e. after the first instability) – as a function of cycle number for samples A and B.

displacement) is much larger than the second ($\Delta E_s \approx 35$ MPa at around $41 \mu\text{m}$ displacement), suggesting that the lower density zone closer to the surface has a greater deleterious effect on the mechanical behavior of the sample. After the second drop the moduli are seen to be increasing again (from 129 to 190 MPa) with increasing displacement for sample B.

Sample B also shows an almost threefold increase in unloading modulus values before the first burst (open symbols, from $E_s = 92$ MPa to 346 MPa). We suspect this large increase to be partly an artifact of the misalignment between the sample surface and the flat punch indenter at the initial stages of loading.

The unloading moduli for sample A show an order of magnitude lower values at similar displacement levels. The moduli in this sample range from ~ 7 MPa, at shallow displacement levels ($\sim 6 \mu\text{m}$ maximum displacement), to ~ 33 MPa, at the largest indentation depth of $66 \mu\text{m}$. This steady increase in the unloading moduli for this sample (as well

as the increase seen in sample B after the second instability) is a likely effect of the increase in density due to compaction of the VACNT matrix under the indenter. Both VACNT samples A and B also show slightly higher values of stiffness at the faster rates, consistent with the typical behavior for viscoelastic solids [69].

We note a particular limitation of our method in calculating the unloading moduli from Eq. (1) as reported in Fig. 4a: Eq. (1) inherently assumes indentation of an elastic half-space, as generally found in monolithic materials [49,70]. This may not be suitable for VACNTs, which are inherently hierarchical in their structure. Moreover, as shown in Fig. 2d for sample B, the VACNT foam can also fracture, further altering the boundary constraints. In spite of these aspects, Fig. 4a helps to underscore the large difference in stiffnesses between the two VACNT samples.

Such differences in unloading moduli between the two samples can be directly attributed to the differences in

tortuosity or waviness in their structures. As shown earlier in Fig. 1, the VACNTs in sample B have a more vertically aligned structure than that of sample A. The longer growth time for sample A results in the distinctive tortuous nature, and the SEM images of this sample show a characteristic waviness with chord lengths of around 7.5–8 μm in their upper cross-section (Fig. 1b). Thus the VACNT network in sample A can be viewed as being already pre-buckled/pre-bent, where the favorable contact energy between the tubes (van der Waals) is balanced by the bending strain energy of their arrangement, resulting in a stable low energy configuration [10]. This structure has a lower mechanical stiffness than the more aligned tubes of sample B. This justification is supported by prior theoretical studies on CNT networks, which have also reported the effective moduli of such networks to be strongly affected by the waviness of the CNT members [36,37]. These studies have shown that an increase in the tortuosity of the fibers (i.e., either a decrease in the chord length, or an increase in the amplitude) can cause a significant decrease in the modulus of the CNT network. The effect was also found to be magnified at lower densities [37]. Our results from Fig. 4a and Table 1 suggest that both these factors – a stronger waviness in sample A and the lower density of sample B – are responsible for the large differences in the moduli of these two samples. The *in situ* tests described in Fig. 2 also suggest that the lower instability (or buckling) stress of sample A could be related to the larger effective buckling length in Sample A ($\sim 60 \mu\text{m}$) as compared to Sample B ($\sim 32 \mu\text{m}$).

Fig. 4b shows the trends in the % recovery (R , Eq. (2)) and Fig. 4c the loss coefficient (η , Eq. (3)) as a function of the load-unload cycle number across the three loading rates. The data for both these figures contain results only for the tests loaded beyond the first instability (or burst). The distinctly higher recovery for sample A ($R \approx 80\%$ for the first cycle) as compared to sample B ($R \approx 22\text{--}40\%$) is evident in Fig. 4b. The loss coefficient η , or fractional energy dissipated during the load-unload cycling process (Fig. 4c), also shows a very similar trend, with sample A demonstrating 2–3 times higher values than sample B.

Interestingly, the two samples show opposite trends with respect to the indentation loading rate. Thus, while in sample A the tests conducted at the slowest 10 nm/s rate are the most permanently deformed (i.e. least recovered), the reverse is true for sample B where the fastest 1000 nm/s tests show the lowest values of R and η , especially in the first cycle (Fig. 4b and c). For VACNT networks showing high resilience, such as sample A, the reduced recovery at slower rates is explained by the greater time allowed for the individual CNTs to come in close contact with one another. These inter-tube interactions are inherently adhesive, due to van der Waals attractions [71]. At the slower indentation rates these attractive forces supersede the elastic recovery process and thus decrease the reversibility of the VACNT structure under the imposed strain, resulting in lower values of R and η . Repeated cycling further exacerbates the process, and the values are seen to drop even more with increasing cycle number. In contrast, at the faster rates there is insufficient interaction time between the CNTs in sample A, and hence much lower adhesion and higher recovery [16].

For sample B, the deformation is dominated by the zone of lower VACNT density present below the surface. Here, the individual CNT struts are also more vertically aligned than in sample A (Fig. 1), making the shear strength in the vertical plane of this sample much lower than that of sample A. Under the high shear forces generated during indentation, sample B experiences a catastrophic shearing-off process where the shear proceeds vertically through the VACNT thickness down to the zone of lower VACNT density. This effect is more drastic along the indenter edges where the indentation shear forces are the largest. In contrast, the slower indentation rates allow more time for the CNTs to reconfigure themselves, and thus help prevent the catastrophic nature of the burst. Hence, in sample B the recovery is higher at slower rates due to the lack of the sudden displacement burst during the loading cycle. The same effect is also seen at faster rates during repeated cycling in sample B (Fig. 4b); at 1000 nm/s the large displacement burst in the first cycle results in very low values of recovery ($R = 22.6 \pm 2\%$). The burst is absent in the subsequent cycles and the recovery improves to $\sim 30\%$ from the 2nd cycle onwards.

We note that the very high recovery ($R \approx 80\%$) of sample A is quite unique for VACNTs under large displacement indentation boundary conditions. Most VACNT systems exhibiting high recoverability have been tested under uniaxial compression, where shear stresses are negligible [1,5,6,15,16]. However, when tested under indentation, some of these same systems have shown very poor recovery ($R < 10\%$) [21,22,72,73], much lower than that of VACNT sample A in this study.

Some prior indentation studies have also noted the catastrophic shear process in the VACNT network. In these reports, the shear proceeds through the entire VACNT thickness, and leads to their virtually-nonexistent material recovery [21,22]. Instead, while sample B in our study suffers from the same shear phenomenon, the presence of the zone of low density in this sample helps to arrest the shear process to only the top section of the VACNT film. As a result, the recoverability of sample B ($R \approx 22\text{--}40\%$) still compares favorably to others reported in literature under indentation.

The viscoelastic indentation responses of the two VACNT films, in terms of the measured values of their storage modulus (E'), loss modulus (E''), and $\tan \delta$, are shown in Fig. 5. In this figure, both the storage and loss moduli for sample A are seen to increase as the indentation depth is increased from 15, 26, 36, 47, 58 to 68 μm . No such increase was noted for sample B. Note that the data for sample B contain values for only the three deeper depths of 47, 58 and 68 μm (see Materials and Methods, Section 2.5).

We find the storage moduli to be frequency independent over the range of frequencies probed for both samples, indicating that the VACNT's elastic deformation is likely due to the same mechanism (probable tube bending) over the range of timescales tested. On the other hand, the loss moduli (and $\tan \delta$) values for sample A show an almost step increase at 10 Hz; above 10 Hz a doubling in the values of these parameters can be seen in Fig. 5b and c. Unfortunately the cut-off frequency (50 Hz) of our instrument prevents further study of this behavior at higher frequencies. Similar to the trends of R and η , such frequency dependence can also be explained

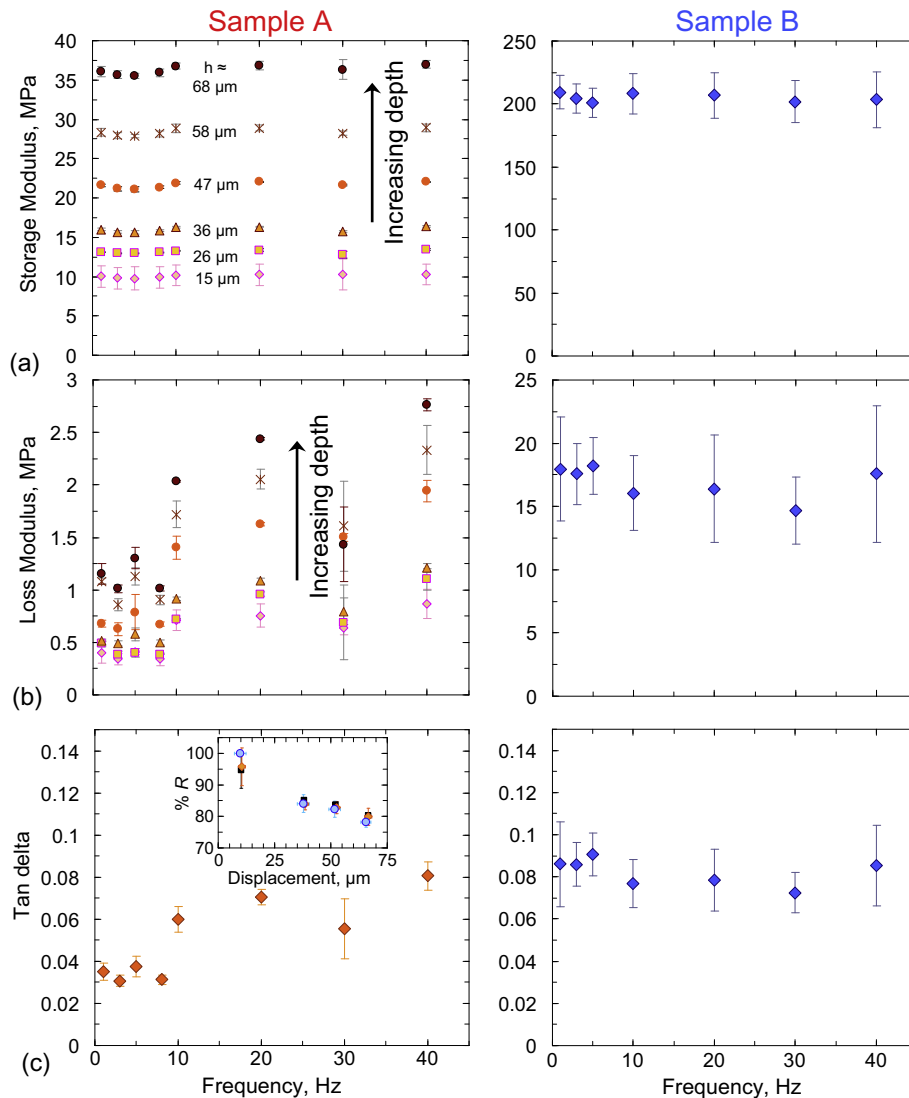


Fig. 5 – Viscoelastic indentation response of the VACNT films at a loading rate of 100 nm/s, in terms of the measured values (average \pm standard deviation) of their (a) storage modulus, (b) loss modulus and (c) $\tan \delta$ values, as a function of frequency. Note the difference in the y-axis scales between samples A and B for (a) and (b). (c inset) % recovery as a function of max displacement before unload for sample A at three different rates, 1000 nm/s (squares), 100 nm/s (diamond) and 10 nm/s (circles).

by the lower interaction time available at higher frequencies. The additional time available at the lower frequencies increases the adhesive interactions between the CNTs, causing a decrease in its ability to dissipate energy.

No such frequency dependence was noticed for the three deeper depths of 47, 58 and 68 μm in sample B. For both samples, the storage moduli E' shown in Fig. 5 match well with the unloading modulus values described earlier in Fig. 4.

3.5. Morphology and recoverability of VACNT systems

The high recoverability in VACNTs and the lack of morphological damage after deformation has significant implications for their use as protective materials and in energy dissipation devices. We have observed that an increased density and tortu-

osity correlates with a significantly higher resilience of the VACNT sample.

In order to understand the factors contributing to the recoverability of VACNTs, we first investigate the density gradient(s) present along the film height. The results from Figs. 1, 2 and 4 appear to indicate that the ability of VACNT sample B to recover under indentation can be strongly affected by the presence of a zone of lower VACNT density $\sim 32 \mu\text{m}$ below the top surface (as we have investigated in more detail elsewhere [45]). While such low density zones have an obvious softening effect on the mechanical properties of this sample, it is still unsure whether this in itself is the sole cause for its lower recoverability. In order to test this effect further, a third VACNT sample was synthesized with a similar reaction time of 7 min resulting in a similar film thickness ($\sim 179 \mu\text{m}$) as

sample B. Care was taken to keep the input rate of the precursor solution constant during synthesis of this third sample, and thus (unlike sample B) no lower density bands were present in this case. The recoverability of this sample (after buckling) was calculated to be $R = 54\%$. Although this value is somewhat higher than that of sample B, it is still significantly lower than the $R \sim 80\%$ seen for sample A. Hence, we can conclude that the presence of the low density bands is not the prime cause for the lower recovery of sample B.

We hypothesize that the lower recovery for VACNT sample B is caused by the more vertical alignment of the constituent CNTs in its matrix, as shown in Fig. 1 [15,74]. As discussed earlier, the vertical plane in this sample is expected to be the plane of lowest shear strength due to the more vertically aligned nature of the constituent CNTs with respect to the loading axis. Once the critical shear stress is attained during loading, the shear-off proceeds catastrophically along this vertical plane through the thickness of the VACNT film down to the underlying low density zone. Thus after buckling there is significant entanglement of the tubes in its matrix. These lateral interconnections between the adjacent CNTs inevitably lead to a strong bundling of the tubes. These interactions are inherently adhesive, due to van der Waals forces, and hence detrimental to the VACNT recovery.

On the other hand in sample A the VACNTs are more tortuous in nature. Such tortuosity/waviness of the CNTs in sample A is expected to cause a higher number of inter-tube contacts in its as grown state, and such interconnections are instrumental in increasing the vertical shear strength of the matrix and hence prevent any catastrophic shear off under indentation. By avoiding the sudden bundling together of its members sample A is able to demonstrate significantly higher recoverability than sample B. The tubes in sample A also have twice the thickness of the CNTs in sample B (see Table 1), and hence the resultant increase in the bending stiffness of the tubes would also aid their elastic recovery process. This matches well with a number of observations in the literature, where reversible VACNT deformation was reported to be more common for thicker tubes (of ≥ 40 nm diameter) [1,25,26].

The above hypothesis is also supported by the results of the viscoelastic measurements of the two samples. In sample A (Fig. 5), we find the storage and loss moduli to increase with increasing indentation depth. Both of these increases can be explained by proportional increase in the number of inter-tube contacts happening at these depths. Theoretical studies have shown that the effective elastic modulus (represented by the storage modulus E') of a stiff fiber network is directly proportional to the number of inter-tube contacts [34,36,37]. Similarly the viscoelastic behavior of VACNTs is thought to be due to the zipping and unzipping of the CNTs upon contact [5,14], and hence an increasing number of interconnections between the tubes should result in a greater viscoelastic response (and a resultant increase in the loss modulus E''). However, since these interactions are also inherently adhesive, it stands to reason that the recovery in this sample should follow the reverse trend, i.e., R should decrease with increasing depth. This can be seen in Fig. 5c (inset) where the recovery gradually decreases from a near complete recovery, $R = 100\%$, at the indentation depth of $h_{\max} = 10 \mu\text{m}$ to $R = 78\%$ at $h_{\max} = 65 \mu\text{m}$,

indicating the detrimental effects of increased VACNT interconnections on their recovery.

The large displacement burst seen in sample B also causes a sudden sharp increase in the CNT lateral connections. We theorize that the catastrophic nature of this shear-off process results in a strong bundling of the contacting CNTs, and a concurrent loss in their alignment. Thus any further increase in the indentation depth beyond the critical shear-off depth causes very little change in the VACNT viscoelastic properties (see data for sample B in Fig. 5). Beyond this critical indentation depth the bundled VACNTs in sample B also lose any frequency dependence in their behavior. These results are similar to those reported in literature for randomly arranged CNTs (i.e. CNT arrays without any preferred vertical alignment, Ref. [5]) where the tan delta and storage and loss moduli were seen to insensitive to the applied frequency.

We note that while these results were found to be repeatable over different sample sets (including the third sample set described above), they are however valid only for the particular growth technique used in this work. The CVD technique for synthesizing VACNTs can be notoriously difficult to control. Changes in the synthesis routines – such as the use of a variable precursor input rate instead of a constant one – can substantially change the resultant VACNT density, alignment, and tortuosity, including their respective variations along the film heights, which affects their recovery [45]. This is reflected in the wide range of recoverability values reported for CVD-VACNTs synthesized using the CVD method [1,5,6,12,15–20]. Experimentally quantifying these parameters continues to be a challenging task.

4. Conclusions

In summary, we report a correlation between certain morphological features of VACNT films, such as the tortuosity of the individual CNTs, and the recoverability of the systems after indentation. We find that the taller VACNT films synthesized for a longer growth time show a higher resilience under indentation. We hypothesize that the higher recovery in the taller films is caused by the increased tortuosity of the constituent CNTs in their network, as well as their higher densities. This combination enables the taller VACNT films to avoid a catastrophic shear failure under the indenter, hence enhancing their recoverability.

Acknowledgments

We acknowledge Prof. Julia R. Greer for helpful discussions and for providing access to testing facilities. SP gratefully acknowledges support from the W.M. Keck Institute for Space Studies Postdoctoral Fellowship program for this work. JRR acknowledges the Army Research Office and the Department of Defense for funding via a National Defense Science & Engineering Graduate fellowship during the course of this work. CD acknowledges support from the Institute for Collaborative Biotechnologies under contract W911NF-09-D-0001 with the Army Research Office. We acknowledge critical support and infrastructure provided for this work by the Kavli Nanoscience Institute at Caltech.

Appendix A. Supplementary data

Supplementary data associated with this article can be found, in the online version, at <http://dx.doi.org/10.1016/j.carbon.2013.06.083>.

REFERENCES

- [1] Cao AY, Dickrell PL, Sawyer WG, Ghasemi-Nejhad MN, Ajayan PM. Super-compressible foamlike carbon nanotube films. *Science* 2005;310(5752):1307–10.
- [2] Misra A, Greer JR, Daraio C. Strain rate effects in the mechanical response of polymer-anchored carbon nanotube foams. *Adv Mater* 2008;20:1–5.
- [3] Cho J, Richards C, Bahr D, Jiao J, Richards R. Evaluation of contacts for a MEMS thermal switch. *J Micromech Microeng* 2008;18(10).
- [4] Cola BA, Xu J, Fisher TS. Contact mechanics and thermal conductance of carbon nanotube array interfaces. *Int J Heat Mass Transfer* 2009;52 (Compendex):3490–503.
- [5] Xu M, Futaba DN, Yamada T, Yumura M, Hata K. Carbon nanotubes with temperature-invariant viscoelasticity from –196 degrees to 1000 degrees C. *Science* 2010;330(6009):1364–8.
- [6] Suhr J, Victor P, Sreekala LCS, Zhang X, Nalamasu O, Ajayan PM. Fatigue resistance of aligned carbon nanotube arrays under cyclic compression. *Nat Nanotechnol* 2007;2(7):417–21.
- [7] Kumar M, Ando Y. Chemical vapor deposition of carbon nanotubes: a review on growth mechanism and mass production. *J Nanosci Nanotechnol* 2010;10(6):3739–58.
- [8] Presser V, Heon M, Gogotsi Y. Carbide-derived carbons – from porous networks to nanotubes and graphene. *Adv Funct Mater* 2011;21(5):810–33.
- [9] Tong T, Zhao Y, Delzeit L, Kashani A, Meyyappan M, Majumdar A. Height independent compressive modulus of vertically aligned carbon nanotube arrays. *Nano Lett* 2008;8(2):511–5.
- [10] Mesarovic SD, McCarter CM, Bahr DF, Radhakrishnan H, Richards RF, Richards CD, et al. Mechanical behavior of a carbon nanotube turf. *Scr Mater* 2007;56(2):157–60.
- [11] Qiu A, Bahr DF, Zbib AA, Bellou A, Mesarovic SD, McClain D, et al. Local and non-local behavior and coordinated buckling of CNT turfs. *Carbon* 2011;49(4):1430–8.
- [12] Zhang Q, Lu YC, Du F, Dai L, Baur J, Foster DC. Viscoelastic creep of vertically aligned carbon nanotubes. *J Phys D-Appl Phys* 2010;43(31):315401. 1–7.
- [13] Deck CP, Flowers J, McKee GSB, Vecchio K. Mechanical behavior of ultralong multiwalled carbon nanotube mats. *J Appl Phys* 2007;101(2):23512. 1–9.
- [14] Pathak S, Cambaz ZG, Kalidindi SR, Swadener JG, Gogotsi Y. Viscoelasticity and high buckling stress of dense carbon nanotube brushes. *Carbon* 2009;47(8):1969–76.
- [15] Xu M, Futaba DN, Yumura M, Hata K. Carbon nanotubes with temperature-invariant creep and creep-recovery from –190 to 970 °C. *Adv Mater* 2011;23(32):3686–91.
- [16] Pathak S, Lim EJ, Pour Shahid Saeed Abadi P, Graham S, Cola BA, Greer JR. Higher recovery and better energy dissipation at faster strain rates in carbon nanotube bundles: an in-situ study. *ACS Nano* 2012;6(3):2189–97.
- [17] Hutchens SB, Hall LJ, Greer JR. In situ mechanical testing reveals periodic buckle nucleation and propagation in carbon nanotube bundles. *Adv Funct Mater* 2010;20(14):2338–46.
- [18] Zbib AA, Mesarovic SD, Lilleodden ET, McClain D, Jiao J, Bahr DF. The coordinated buckling of carbon nanotube turfs under uniform compression. *Nanotechnology* 2008;19(17):175704. 1–7.
- [19] Cao C, Reiner A, Chung C, Chang S-H, Kao I, Kukta RV, et al. Buckling initiation and displacement dependence in compression of vertically aligned carbon nanotube arrays. *Carbon* 2011;49(10):3190–9.
- [20] Yaglioglu O. Carbon Nanotube Based Electromechanical Probes - PhD Thesis. Massachusetts Institute of Technology, PhD., 2007.
- [21] Pour Shahid Saeed Abadi P, Hutchens S, Taphouse JH, Greer JR, Cola BA, Graham S. The effect of morphology on the micro-compression response of carbon nanotube forests. *Nanoscale* 2012;4(11):3373–80.
- [22] Pathak S, Mohan N, Pour Shahid Saeed Abadi P, Graham S, Cola BA, Greer JR. Compressive response of vertically aligned carbon nanotube films gleaned from in-situ flat punch indentations. *J Mater Res: Focus Issue on De Novo Carbon Nanomater* 2013;28(7). <http://dx.doi.org/10.1557/jmr.2012.366>.
- [23] Lu YC, Joseph J, Zhang Q, Maschmann MR, Dai L, Baur J. Large-displacement indentation testing of vertically aligned carbon nanotube arrays. *Exp Mech* 2012. <http://dx.doi.org/10.1007/s11340-012-9609-1>. in press.
- [24] Andrews R, Jacques D, Rao AM, Derbyshire F, Qian D, Fan X, et al. Continuous production of aligned carbon nanotubes: a step closer to commercial realization. *Chem Phys Lett* 1999;303(5–6):467–74.
- [25] Raney JR, Misra A, Daraio C. Tailoring the microstructure and mechanical properties of arrays of aligned multiwall carbon nanotubes by utilizing different hydrogen concentrations during synthesis. *Carbon* 2011;49:3631–8. Compendex.
- [26] Raney JR, Fraternali F, Amendola A, Daraio C. Modeling and in situ identification of material parameters for layered structures based on carbon nanotube arrays. *Compos Struct* 2011;93(11):3013–8.
- [27] Yaglioglu O, Cao A, Hart AJ, Martens R, Slocum AH. Wide range control of microstructure and mechanical properties of carbon nanotube forests: a comparison between fixed and floating catalyst CVD techniques. *Adv Funct Mater* 2012;22(23):5028–37.
- [28] Bedewy M, Meshot ER, Guo H, Verploegen EA, Lu W, Hart AJ. Collective mechanism for the evolution and self-termination of vertically aligned carbon nanotube growth. *J Phys Chem C* 2009;113(48):20576–82.
- [29] Bradford PD, Wang X, Zhao H, Zhu YT. Tuning the compressive mechanical properties of carbon nanotube foam. *Carbon* 2011;49(8):2834–41.
- [30] Al-Khedher MA, Pezeshki C, McHale JL, Knorr FJ. Quality classification via Raman identification and SEM analysis of carbon nanotube bundles using artificial neural networks. *Nanotechnology* 2007;18(35).
- [31] Malik H, Stephenson KJ, Bahr DF, Field DP. Quantitative characterization of carbon nanotube turf topology by SEM analysis. *J Mater Sci* 2011;46(9):3119–26.
- [32] McCarter CM, Richards RF, Mesarovic SD, Richards CD, Bahr DF, McClain D, et al. Mechanical compliance of photolithographically defined vertically aligned carbon nanotube turf. *J Mater Sci* 2006;41(23):7872–8.
- [33] Gao Y, Kodama T, Won Y, Dogbe S, Pan L, Goodson KE. Impact of nanotube density and alignment on the elastic modulus near the top and base surfaces of aligned multi-walled carbon nanotube films. *Carbon* 2012;50(10):3789–98.
- [34] Astrom JA, Krasheninnikov AV, Nordlund K. Carbon nanotube mats and fibers with irradiation-improved mechanical characteristics: a theoretical model. *Phys Rev Lett* 2004;93(21):215503. 1–4.
- [35] Cox HL. Elasticity and strength of paper and other fibrous materials. *Br J Appl Phys* 1952;3(3):72–9.

- [36] Berhan L, Yi YB, Sastry AM, Munoz E, Selvidge M, Baughman R. Mechanical properties of nanotube sheets: alterations in joint morphology and achievable moduli in manufacturable materials. *J Appl Phys* 2004;95(8):4335–45.
- [37] Berhan L, Yi YB, Sastry AM. Effect of nanorope waviness on the effective moduli of nanotube sheets. *J Appl Phys* 2004;95(9):5027–34.
- [38] Maschmann MR, Zhang Q, Wheeler R, Du F, Dai L, Baur J. In situ SEM Observation of column-like and foam-like CNT array nanoindentation. *ACS Appl Mater Interfaces* 2011;3(3):648–53.
- [39] Waters JF, Riester L, Jouzi M, Guduru PR, Xu JM. Buckling instabilities in multiwalled carbon nanotubes under uniaxial compression. *Appl Phys Lett* 2004;85(10):1787–9.
- [40] Waters JF, Guduru PR, Jouzi M, Xu JM, Hanlon T, Suresh S. Shell buckling of individual multiwalled carbon nanotubes using nanoindentation. *Appl Phys Lett* 2005;87:103109. 1–3.
- [41] Kim J-Y, Greer JR. Tensile and compressive behavior of gold and molybdenum single crystals at the nano-scale. *Acta Materialia* 2009;57:5245–53. Compendex.
- [42] Pathak S, Lim EJ, Pour Shahid Saeed Abadi P, Graham S, Cola BA, Greer JR. Higher recovery and better energy dissipation at faster strain rates in carbon nanotube bundles: an in-situ study. *ACS Nano* 2012. <http://dx.doi.org/10.1021/nn300376j>.
- [43] Malek Abbaslou RM, Soltan J, Dalai AK. The effects of carbon concentration in the precursor gas on the quality and quantity of carbon nanotubes synthesized by CVD method. *Appl Catal A: General* 2010;372(2):147–52.
- [44] Maghrebi M, Khodadadi AA, Mortazavi Y, Rahimi M, Sane A, Tsakadze Z, et al. The effects of carrier gas and liquid feed flow rates on longitudinal patterns of CNT growth. *Mater Chem Phys* 2010;124(2–3):1139–45.
- [45] Raney JR, Wang RY, Daraio C. Control of microstructural heterogeneities in carbon nanotube foams. *Carbon* 2012. in review.
- [46] Li X, Cao A, Jung YJ, Vajtai R, Ajayan PM. Bottom-up growth of carbon nanotube multilayers: unprecedented growth. *Nano Lett* 2005;5(10):1997–2000.
- [47] Pinault M, Pichot V, Khodja H, Launois P, Reynaud C, Mayne-L'Hermite M. Evidence of sequential lift in growth of aligned multiwalled carbon nanotube multilayers. *Nano Lett* 2005;5(12):2394–8.
- [48] Johnson KL. *Contact Mechanics*. Cambridge: Cambridge University Press; 1987.
- [49] Oliver WC, Pharr GM. Improved technique for determining hardness and elastic modulus using load and displacement sensing indentation experiments. *J Mater Res* 1992;7(6):1564–80.
- [50] Tu JP, Jiang CX, Guo SY, Fu MF. Micro-friction characteristics of aligned carbon nanotube film on an anodic aluminum oxide template. *Mater Lett* 2004;58:1646–9. Copyright 2004, IEE.
- [51] Tu JP, Zhu LP, Hou K, Guo SY. Synthesis and frictional properties of array film of amorphous carbon nanofibers on anodic aluminum oxide. *Carbon* 2003;41:1257–63. Compendex.
- [52] Bhushan B, Xing L, Jungen A, Hierold C. Adhesion and friction of a multiwalled carbon nanotube sliding against single-walled carbon nanotube. *Phys Rev B (Condens Matter Mater Phys)* 2008;77(16):165428. 1.
- [53] Lattanzi L, Raney JR, De Nardo L, Misra A, Daraio C. Nonlinear viscoelasticity of freestanding and polymer-anchored vertically aligned carbon nanotube foams. *J Appl Phys* 2012;111.
- [54] Deshpande VS, Fleck NA. Isotropic constitutive models for metallic foams. *J Mech Phys Solids* 2000;48(6–7):1253–83.
- [55] Ashby MF. *Materials Selection in Mechanical Design*. Butterworth-Heinemann; 2005.
- [56] Herbert EG, Oliver WC, Pharr GM. Nanoindentation and the dynamic characterization of viscoelastic solids. *J Phys D Appl Phys* 2008;41(7):074021. 1.
- [57] Herbert EG, Oliver WC, Lumsdaine A, Pharr GM. Measuring the constitutive behavior of viscoelastic solids in the time and frequency domain using flat punch nanoindentation. *J Mater Res* 2009;24(3):626–37.
- [58] Wright WJ, Maloney AR, Nix WD. An improved analysis for viscoelastic damping in dynamic nanoindentation. *Int J Surf Sci Eng* 2007;1(2–3):274–92.
- [59] Wright WJ, Nix WD. Storage and loss stiffnesses and moduli as determined by dynamic nanoindentation. *J Mater Res* 2009;24(3):863–71.
- [60] Pathak S, Gregory Swadener J, Kalidindi SR, Courtland H-W, Jepsen KJ, Goldman HM. Measuring the dynamic mechanical response of hydrated mouse bone by nanoindentation. *J Mech Behav Biomed Mater* 2011;4:34–43. Compendex.
- [61] Hutchens SB, Needleman A, Greer JR. Analysis of uniaxial compression of vertically aligned carbon nanotubes. *J Mech Phys Solids* 2011;59(10):2227–37.
- [62] Jackson JJ, Puzetzy AA, More KL, Rouleau CM, Eres G, Geohegan DB. Pulsed growth of vertically aligned nanotube arrays with variable density. *ACS Nano* 2010;4(12):7573–81.
- [63] Li X, Ci L, Kar S, Soldano C, Kilpatrick SJ, Ajayan PM. Densified aligned carbon nanotube films via vapor phase infiltration of carbon. *Carbon* 2007;45(4):847–51.
- [64] Sudheer Kumar P, Ramchandra S, Ramamurthy U. Effect of displacement-rate on the indentation behavior of an aluminum foam. *Mater Sci Eng A* 2003;347(1–2):330–7.
- [65] Gibson LJ, Ashby MF. *Cellular Solids: Structure and Properties*. Cambridge, UK: Cambridge University Press; 1999.
- [66] Fleck NA, Otoyoy H, Needleman A. Indentation of porous solids. *Int J Solids Struct* 1992;29(13):1613–36.
- [67] Gibson LJ. Mechanical behavior of metallic foams. *Annu Rev Mater Sci* 2000;30:191–227. Compendex.
- [68] Pantano A, Parks DM, Boyce MC. Mechanics of deformation of single- and multi-wall carbon nanotubes. *J Mech Phys Solids* 2004;52(4):789–821.
- [69] Lakes RS. *Viscoelastic Solids*. CRC Press; 1998.
- [70] Doerner MF, Nix WD. A method for interpreting the data from depth-sensing indentation instruments. *J Mater Res* 1986;1(4):601–9.
- [71] Ruoff RS, Tersoff J, Lorents DC, Subramoney S, Chan B. Radial deformation of carbon nanotubes by van der waals forces. *Nature* 1993;364(6437):514–6.
- [72] Maschmann MR, QiuHong Z, Feng D, Liming D, Baur J. Length dependent foam-like mechanical response of axially indented vertically oriented carbon nanotube arrays. *Carbon* 2011;49(2):386–97.
- [73] Lu YC, Joseph J, Zhang Q, Maschmann MR, Dai L, Baur J. Large-displacement indentation of vertically aligned carbon nanotube arrays. *Exp Mech* 2012. <http://dx.doi.org/10.1007/s11340-012-9609-1>. in press.
- [74] Ge L, Ci L, Goyal A, Shi R, Mahadevan L, Ajayan PM, et al. Cooperative adhesion and friction of compliant nanohairs. *Nano Lett* 2010;10(11):4509–13.